The Cospectrum of Stress-Carrying Turbulence in the Presence of Surface Gravity Waves

JOHN TROWBRIDGE AND MALCOLM SCULLY

Woods Hole Oceanographic Institution, Woods Hole, Massachusetts

CHRISTOPHER R. SHERWOOD

U.S. Geological Survey, Woods Hole, Massachusetts

ABSTRACT

The cospectrum of the horizontal and vertical turbulent velocity fluctuations, an essential tool for understanding measurements of the turbulent Reynolds shear stress, often departs in the ocean from the shape that has been established in the atmospheric surface layer. Here, we test the hypothesis that this departure is caused by advection of standard boundary layer turbulence by the random oscillatory velocities produced by surface gravity waves. The test is based on a model with two elements. The first is a representation of the spatial structure of the turbulence, guided by rapid distortion theory, and consistent with the one-dimensional cospectra that have been measured in the atmosphere. The second model element is a map of the spatial structure of the turbulence to the temporal fluctuations measured at fixed sensors, assuming advection of frozen turbulence by the velocities associated with surface waves. The model is adapted to removal of the wave velocities from the turbulent fluctuations using spatial filtering. The model is tested against previously published laboratory measurements under wave-free conditions and two new sets of measurements near the seafloor in the coastal ocean in the presence of waves. Although quantitative discrepancies exist, the model captures the dominant features of the laboratory and field measurements, suggesting that the underlying model physics are sound.

1. Introduction

The cospectrum of the horizontal and vertical components of the turbulent velocity is an essential tool for understanding the turbulent Reynolds shear stress and interpreting stress measurements. The cospectrum provides an estimate of the dominant stress-carrying turbulent length scale (e.g., Kaimal et al. 1972), an assessment of whether the stress-carrying scales have been resolved, and an indication of contamination of stress estimates by spurious contributions from sensor noise.

In the atmospheric surface layer, the shape of the stress-carrying cospectrum is well established for horizontally homogeneous flows over fixed surfaces with uniform roughness elements that are small in comparison with the distance above the boundary. In this environment, the turbulent velocity fluctuations are much smaller than the mean velocity. The standard procedure is to (i) obtain time series measurements of u'_1 and u'_3 at a fixed point; (ii) assume that the turbulence is frozen (e.g., Tennekes and Lumley 1972; Monin and Yaglom 1975), so that each time series can be interpreted as a one-dimensional spatial series using the mapping $x_1 = U_1 t$; and (iii) compute the one-dimensional wavenumber cospectrum of the spatial series u'_1 and u'_3. Kaimal et al. (1972) showed that the cospectrum $F_{13}(k_1)$ computed in this way from atmospheric measurements is represented by an expression similar to

$$F_{13}(k_1) = \frac{2}{3} \frac{\overline{u'_1 u'_3} \lambda}{(1 + |k_1| \lambda)^{7/3}}, \tag{1}$$

with some discrepancies at low wavenumbers in unstable stratification. Here, $\mathbf{x} = (x_1, x_2, x_3)$ is the position, with x_3 as the distance above the boundary and x_1 aligned with the turbulent Reynolds shear stress, assumed to be aligned with the mean current; $\mathbf{k} = (k_1, k_2, k_3)$ is the wavenumber; t is the time; $\mathbf{U} = (U_1, U_2, U_3) = (U_1, 0, 0)$ is the mean velocity; $\mathbf{u}'(\mathbf{x}, t) = (u'_1, u'_2, u'_3)$ is the turbulent component of the velocity; overbars denote mean values; $\overline{u'_1 u'_3}$ is the

covariance of the streamwise and vertical components of the turbulent velocity vector, proportional to the turbulent Reynolds shear stress; the factor 2/3 achieves $\int_{-\infty}^{+\infty} F_{13}(k_1) dk_1 = \overline{u'_1 u'_3}$; the exponent 7/3 follows from scaling and dimensional considerations at high wavenumber (e.g., Wyngaard and Cote 1972); and λ is a turbulent length scale, approximately equal to $1.5x_3$ in neutral or unstable stratification and dependent on x_3 and the Monin–Obukhov length in stable stratification (Kaimal et al. 1972). The assumption that the turbulent Reynolds shear stress and the mean velocity are aligned is consistent with the standard wall layer assumption that the distance above the boundary is small in comparison with the boundary layer thickness, so that the processes that might cause misalignment (Ekman veering and transient forcing) are negligible.

In the ocean, surface waves complicate frequency cospectra computed from measurements obtained by point sensors at fixed positions, even in the absence of dynamical wave–current interactions, such as the steady streaming (Longuet-Higgins 1953), Langmuir circulations (Craik and Leibovich 1976), or the turbulent wave–current boundary layer (Grant and Madsen 1979), because of at least two kinematical effects. First, even if the wave velocities are filtered perfectly from measurements obtained by a point sensor at a fixed position, advection of the turbulence by the wave velocities distorts the frequency spectrum computed from the filtered measurements of the turbulent velocity (Lumley and Terray 1983). Second, even a small uncertainty in the sensor orientation relative to the principal axes of the velocities associated with waves can create large uncertainties in stress estimates obtained from measurements by a single sensor (Grant and Madsen 1986) because the velocity variances produced by the surface waves are often orders of magnitude larger than those associated with boundary layer turbulence.

Lumley and Terray (1983) analyzed the first effect (advection of turbulence by velocities associated with waves), assuming frozen turbulence, statistically independent waves and turbulence, and linear waves with Gaussian statistics. The Lumley and Terray analysis maps the spatial structure of the turbulence to the temporal fluctuations that are measured by a fixed sensor in the presence of waves. Terray et al. (1996), Trowbridge and Elgar (2001), Feddersen et al. (2007), Gerbi et al. (2009), Feddersen (2012), Scully et al. (2016), and others have combined this analysis with an isotropic model of the underlying turbulence to describe high-frequency turbulent autospectra for estimation of the turbulent energy dissipation rate. Gerbi et al. (2008) and Rosman and Gerbi (2017) used the Lumley and Terray (1983) analysis and a turbulence model similar

to (1) to simulate the effects of wave advection on the stress-carrying turbulent cospectrum for the case in which the advection by the current and waves is solely in the x_1 direction.

Trowbridge (1998) proposed mitigation of the second effect (sensitivity of stress measurements to uncertainty in the sensor orientation in the presence of strong waves and weak turbulence) by differencing measurements obtained by two sensors separated by a distance larger than the correlation scale of the turbulence but much smaller than the surface wavelength. The analysis indicates that $(1/2)\overline{\Delta u_1 \Delta u_3}$ is an approximately wave-free measurement of $\overline{u'_1 u'_3}$ if $(\mathbf{k}_w \cdot \Delta \mathbf{x})^2 \theta \overline{\tilde{u}^2} \ll \overline{u'_1 u'_3}$. Here, $\Delta \mathbf{u}(t) = (\Delta u_1, \Delta u_2, \Delta u_3) = \mathbf{u}(\mathbf{x} + \Delta \mathbf{x}, t) - \mathbf{u}(\mathbf{x}, t)$ is the velocity difference, $\Delta \mathbf{x}$ is the sensor separation, $\mathbf{k}_w$ is the dominant wavenumber of the surface waves that produce motions penetrating downward to the measurement depth, θ is the misalignment between the sensor orientation and the principal axes of the wave velocities, and $\overline{\tilde{u}^2}$ is the wave velocity variance. Velocity differences can be interpreted as either high-pass spatial filtering or a spatial structure function and have been applied in the surfzone (Trowbridge and Elgar 2001), incorporated with temporal filtering (Shaw and Trowbridge 2001; Feddersen and Williams 2007; Ruessink 2010), and extended to spatial arrays of sensors (Trowbridge and Elgar 2003). However, the Trowbridge (1998) paper and subsequent work does not describe the frequency cospectrum of Δu_1 and Δu_3.

To enable analysis and interpretation of stress measurements based on the differencing method, this study proposes and tests a model of the frequency cospectrum of time series of Δu_1 and Δu_3 that are measured by a pair of fixed sensors in the presence of surface waves. The model has two elements. The first is a representation of the spatial structure of the turbulence, guided by the rapid distortion solution for initially isotropic turbulence in mean shear (Townsend 1980) and consistent with the one-dimensional wavenumber cospectrum equation [(1)]. The rapid distortion solution provides a dynamically consistent framework and has proven successful, in spite of its simplicity, in other contexts (e.g., Savill 1987; Hunt and Carruthers 1990; Cambon and Scott 1999). The second model element is the Lumley and Terray (1983) mapping of the spatial structure of the turbulence to the temporal fluctuations measured by fixed sensors in the presence of waves, adapted to the difference between measurements obtained by two fixed sensors. The proposed model is tested against previously reported measurements of the spatial correlation function (the Fourier transform of the cospectrum) under wave-free conditions in the laboratory and against new measurements near the seafloor over the inner continental

shelf off of Martha's Vineyard, in which the velocities associated with surface waves are much larger than those associated with turbulence. The following presents methods (section 2), results (section 3), a discussion (section 4), and a summary and conclusions (section 5), followed by two appendices with model details.

2. Methods

a. Model of the spatial structure of the turbulence

The spatial structure of locally spatially homogeneous, stress-carrying turbulence (Batchelor 1953; Tennekes and Lumley 1972; Monin and Yaglom 1975) is described by the three-dimensional spatial correlation function $R_{13}(\mathbf{r})$, defined by

$$R_{13}(\mathbf{r}) = \overline{u_1'(\mathbf{x}, t) u_3'(\mathbf{x} + \mathbf{r}, t)}, \tag{2}$$

or alternatively its three-dimensional Fourier transform, the wavenumber spectrum $\Phi_{13}(\mathbf{k})$:

$$\Phi_{13}(\mathbf{k}) = \frac{1}{(2\pi)^3} \int R_{13}(\mathbf{r}) e^{-\iota \mathbf{k} \cdot \mathbf{r}} \, d\mathbf{r}. \tag{3}$$

The one-dimensional wavenumber spectrum $F_{13}(k_1)$ in (1) is related to $\Phi_{13}(\mathbf{k})$ in (3) by

$$F_{13}(k_1) = \mathrm{Re} \int_{-\infty}^{+\infty} \int_{-\infty}^{+\infty} \Phi_{13}(\mathbf{k}) \, dk_2 \, dk_3. \tag{4}$$

Here, $\mathbf{r} = (r_1, r_2, r_3)$ is the displacement, $\iota = \sqrt{-1}$ is the imaginary unit, and the integral in (3) is over all of the three-dimensional $\mathbf{r}$ space.

Because of intended applications near the seafloor, the present study does not require specification of $\Phi_{13}(\mathbf{k})$, which depends on all three components of the wavenumber, but instead only $\mathrm{Re} \int_{-\infty}^{+\infty} \Phi_{13}(\mathbf{k}) dk_3$, which depends on k_1 and k_2 but not k_3. A simple model, similar to a more complicated model based on rapid distortion theory (appendix A), is

$$\mathrm{Re} \int_{-\infty}^{+\infty} \Phi_{13}(\mathbf{k}) dk_3 = \frac{455}{81} \frac{\overline{u_1' u_3'} \lambda^4 k_2^2}{(1 + \lambda|k_1| + \lambda|k_2|)^{16/3}}. \tag{5}$$

Substitution of (5) into (4) and evaluation of the k_2 integral yields (1), so that (5) is consistent with one-dimensional cospectra in the atmosphere. Inverse Fourier transformation of (3) with (5) determines, for $r_3 = 0$, the even part of $R_{13}(\mathbf{r})$, defined by

$$R_{13}^E(\mathbf{r}) = \frac{1}{2}[R_{13}(\mathbf{r}) + R_{13}(-\mathbf{r})] = \int \mathrm{Re}[\Phi_{13}(\mathbf{k})] e^{\iota \mathbf{k} \cdot \mathbf{r}} \, d\mathbf{k}. \tag{6}$$

The parameters in the model equation [(5)] are $\overline{u_1' u_3'}$ and λ.

b. Model of the temporal statistics of velocity differences

The covariations of the temporal fluctuations of the velocity differences $\Delta u_1(t)$ and $\Delta u_3(t)$ are described under stationary conditions by the correlation function $\rho_{\Delta u_1 \Delta u_3}(\tau)$, defined by

$$\rho_{\Delta u_1 \Delta u_3}(\tau) = \overline{\Delta u_1(t) \Delta u_3(t + \tau)}, \tag{7}$$

or alternatively its Fourier transform, the cross-spectrum $S_{\Delta u_1 \Delta u_3}(\omega)$, given by

$$S_{\Delta u_1 \Delta u_3}(\omega) = \frac{1}{2\pi} \int_{-\infty}^{+\infty} \rho_{\Delta u_1 \Delta u_3}(\tau) e^{-\iota \omega \tau} \, d\tau. \tag{8}$$

Here, τ is the temporal lag and ω is the radian frequency.

In the present study, the mapping of (2) and (3), representing the spatial structure of the turbulence, to (7) and (8), representing the temporal fluctuations measured by fixed sensors, is based on the framework proposed by Lumley and Terray (1983). In the present study, the scales are assumed to be such that the velocities are dominated by the current and waves, but the statistics (7) and (8) of the velocity differences are dominated by the turbulence (Trowbridge 1998). Under these conditions, $\rho_{\Delta u_1 \Delta u_3}(\tau)$ is related to $\Phi_{13}(\mathbf{k})$ (as shown in appendix B) by

$$\rho_{\Delta u_1 \Delta u_3}(\tau) = 2 \int \Phi_{13}(\mathbf{k}) e^{\iota \mathbf{k} \cdot \mathbf{U} \tau} \exp\left[-\frac{k_m k_n \tau^2}{2} \int_{-\infty}^{+\infty} \frac{\sin^2(\sigma \tau/2)}{(\sigma \tau/2)^2} S_{\tilde{u}_m \tilde{u}_n}(\sigma) \, d\sigma \right] [1 - \cos(\mathbf{k} \cdot \Delta \mathbf{x})] \, d\mathbf{k}. \tag{9}$$

Here, the integral is over all of the three-dimensional $\mathbf{k}$ space, σ is a dummy integration variable for the radian frequency, $S_{\tilde{u}_m \tilde{u}_n}(\sigma)$ is the frequency cross spectrum of the m and n components of the wave velocity $\tilde{\mathbf{u}}(t) = (\tilde{u}_1, \tilde{u}_2, \tilde{u}_3)$, and the tensor summation convention applies, that is, the argument of the exponential function is understood to be

summed over all three values of the repeated indices m and n (e.g., Jeffreys 1931). Equation (9) is equivalent to the general results (2.2), (2.3), and (2.6) in Lumley and Terray (1983), except for the present representation in terms of wave velocities, instead of displacements, and the factor $2[1 - \cos(\mathbf{k} \cdot \Delta\mathbf{x})]$, which results from differencing the spatially separated velocities. The correlation $\rho_{\Delta u_1 \Delta u_3}(0)$ at zero lag varies from zero at $\Delta\mathbf{x} = 0$ to $2\overline{u'_1 u'_3}$ for $|\Delta\mathbf{x}|$ larger than the spatial correlation scale of the turbulence, consistent with the behavior of a spatial structure function. Note that the representation in terms of $S_{\bar{u}_m \bar{u}_n}(\sigma)$ accounts for both the frequency and directional distribution of the surface waves.

In the present application, the sensor separation is horizontal, and proximity to the seafloor dictates that the vertical component of the mean velocity and the vertical velocities associated with surface waves make a negligible contribution to (9). For these conditions, model equations (5), (8), and (9) determine $\mathrm{Re}[S_{\Delta u_1 \Delta u_3}(\omega)]$, given $\Delta\mathbf{x}$, λ, U_1, $\overline{u'_1 u'_3}$, and $S_{\bar{u}_m \bar{u}_n}$ for m, $n = 1$, 2. To implement the model given these quantities, one creates arrays of k_1 and k_2, computes $\mathrm{Re} \int_{-\infty}^{+\infty} \Phi_{13}(\mathbf{k}) \, dk_3$ using (5), creates an array of τ, computes $\rho_{\Delta u_1 \Delta u_3}(\tau)$ using (9), and computes $\mathrm{Re}(S_{\Delta u_1 \Delta u_3})$ using (8).

c. Laboratory measurements

Tritton (1967) and Ganapathisubramani et al. (2005) reported measurements of the spatial covariance functions $R_{13}(r_1, 0, 0)$ and $R_{13}(0, r_2, 0)$ in unstratified turbulent boundary layers under wave-free conditions in laboratory wind tunnels. The measurements in the two studies were under similar conditions and agree well with each other. The present study uses the Ganapathisubramani et al. (2005) measurements because these, unlike the Tritton (1967) measurements, were obtained symmetrically for positive and negative r_1 and r_2, permitting extraction of the even part $R_{13}^E(\mathbf{r})$ of the covariance functions, the only part described by the present model. Ganapathisubramani et al. (2005) reported measurements at two heights under one set of conditions. The model data comparison is based on $R_{13}^E(\mathbf{r}) / \overline{u'_1 u'_3} = R_{13}^E(\mathbf{r}) / R_{13}^E(0)$.

The elevation at the uppermost laboratory measurements did not satisfy $x_3 \ll \delta$, required for wall layer scaling, where δ is the boundary layer thickness. Thus, λ at this elevation plausibly depends not only on x_3 but also on δ. To provide a predictive relationship, λ is set to $1.5x_3$ for $x_3 < 0.15\delta$, consistent with (1), and to 0.23δ for $x_3 \geq 0.15\delta$, in analogy with the turbulent mixing length, which is observed to be proportional to x_3 for $x_3 \ll \delta$ and approximately constant for $x_3 > 0.15\delta$ (e.g., Schlichting and Gersten 2000).

d. Field measurements

Field measurements were made on the inner continental shelf south of Martha's Vineyard, Massachusetts, near the Martha's Vineyard Coastal Observatory (MVCO). The study site is exposed to the Atlantic Ocean and has a predominantly sandy seafloor that fines with depth and has alternating ribbons of fine sand with small ripples and coarse sand with large ripples (Fig. 1). A quadpod (Fig. 2) was placed from early July to late August 2014 at site QS1, at a mean depth of 16.2 m, and from mid-November 2014 to mid-January 2015 at site QS3, at a mean depth of 17.9 m (Fig. 1). The seafloor at QS1 was gravelly coarse sand (median size from a grab sample = 790 μm) with large orbital ripples [wavelength from the sonar = 0.5 to 0.8 m; heights estimated from the Aquatec acoustic backscatter sensor (ABSS) = 0.08 to 0.15 m]. At QS3, no grab sample was taken, but the sonar shows small anorbital ripples (wavelength 0.10–0.15 m and height~0.02 m), indicating fine sand, consistent with the sidescan sonar imagery (Fig. 1).

The quadpod supported (i) two Nortek Vector acoustic Doppler velocimeter (ADVs) for measuring the current and making direct covariance estimates of the stress; (ii) a downward-looking Nortek Aquadopp acoustic Doppler profiler and an ABSS for measuring the vertical structure of the current, the suspended sediment concentration in the bottom meter of the water column, and ripple heights; (iii) an upward-looking, five-beam Nortek Signature acoustic Doppler current profiler (ADCP) for measuring waves and currents and detecting the presence and characteristics of Langmuir circulations (Gargett et al. 2004; Gargett and Wells 2007); (iv) temperature and conductivity sensors (RBR Solo-Ts and Sea-Bird MicroCATs) to measure the stratification; and (v) downward-looking, Imagenex, rotary, azimuth-drive, pencil-beam and rotary fan-beam sonars to quantify bed forms. The instrument cases were mounted at the top of the quadpod (Fig. 2), separated from the sample volumes of the velocity sensors.

The present analysis is based on data from the ADVs, which provided measurements of the currents, wave velocities, and turbulence, and the temperature and conductivity sensors, which provided estimates of the stratification. The ADV sample volumes were approximately 0.50 m above bottom and separated horizontally by 1.20 m. The ADV separation (Fig. 3) was roughly along isobath during the first deployment (QS1) and at an angle of approximately 60° with respect to the isobaths during the second deployment (QS3). The ADVs sampled synchronously at 32 Hz, with 28-min bursts recorded each half hour. The temperature and conductivity sensors were at heights of approximately 0.24,
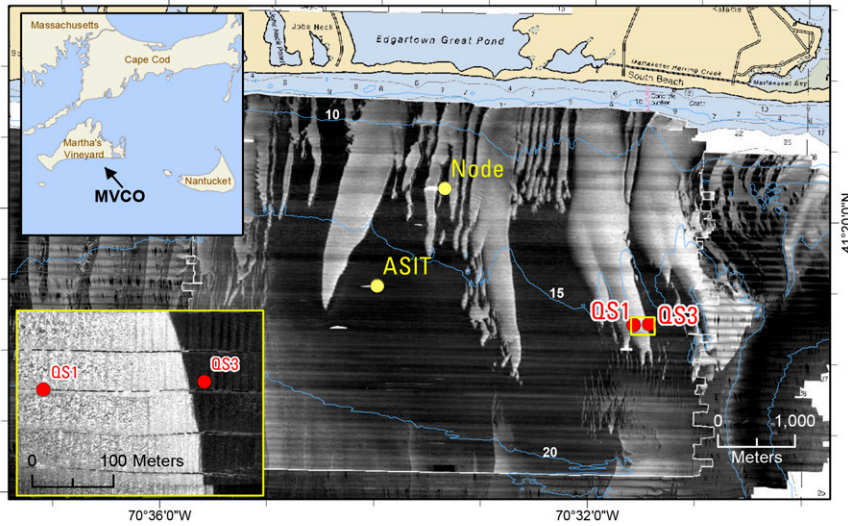
FIG. 1. Map of the coastal ocean south of Martha's Vineyard, Massachusetts, with overlain sidescan sonar imagery (Denny et al. 2009; Ackerman et al. 2016), indicating selected MVCO infrastructure [the seafloor node and the Air–Sea Interaction Tower (ASIT)] and the quadpod deployment sites QS1 and QS3. Bright and dark sidescan images correspond to coarse and fine seafloor sediments, respectively.

1.44, and 2.23 m above bottom. The temperature sensors sampled at 1 Hz and the conductivity sensors at 3 min.

The ADV data were quality controlled by rejecting measurements with correlations of successive acoustic pings less than 80%, similar to criteria recommended by Elgar et al. (2005) and Feddersen (2010) for applications in the surfzone. Rejected measurements were replaced with the burst mean of the retained measurements and bursts with more than 10% rejected were excluded from further analysis. This procedure resulted in exclusion of 41% of the bursts from the first deployment (QS1) and 4% from the second deployment (QS3). The large fraction of rejected bursts during the first deployment resulted from electronic noise from a source that was not identified despite extensive communications with the manufacturer.

For each 28-min burst, the quality-controlled ADV measurements were rotated into coordinates with x_1 aligned with the mean velocity. The spectra $S_{\tilde{u}_m\tilde{u}_n}$ (for m, $n = 1, 2$) and the cospectrum $\mathrm{Re}(S_{\Delta u_1 \Delta u_3})$ were estimated by computing periodograms and smoothing in the frequency domain over 16 bands using a rectangular (Daniell) window, and confidence limits for $\mathrm{Re}(S_{\Delta u_1 \Delta u_3})$ were calculated from standard expressions (e.g., Priestley 1981). The model parameters $\overline{u_1' u_3'}$ and λ were estimated for each burst by minimizing the sum of the squared differences between the measured and modeled cospectrum, subject to the constraint that the integral of the cospectral density, over the range of frequencies resolved by the measurements, was equal for the model and the measurements. The resulting model data comparison tests the model

representation of the cospectral shape. Bursts with positive $\overline{u_1' u_3'}$ (corresponding to negative seafloor drag) and $-\overline{u_1' u_3'}/U_1^2 > 0.02$ (corresponding to seafloor drag coefficients an order of magnitude larger than the overall average of approximately 3×10^{-3}) were excluded from the analysis. These measures resulted in rejection of 4% and 6% of the bursts from the first and second deployments, respectively.

Effects of stable stratification were quantified using the Ozmidov scale $L_O = \varepsilon^{1/2}/N^{3/2}$ (e.g., Phillips 1980), an upper bound imposed by stratification on the scale of the turbulent eddies. Here, N is the buoyancy frequency,
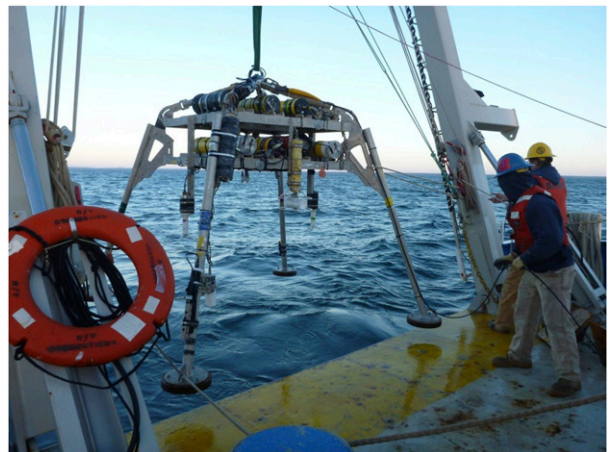

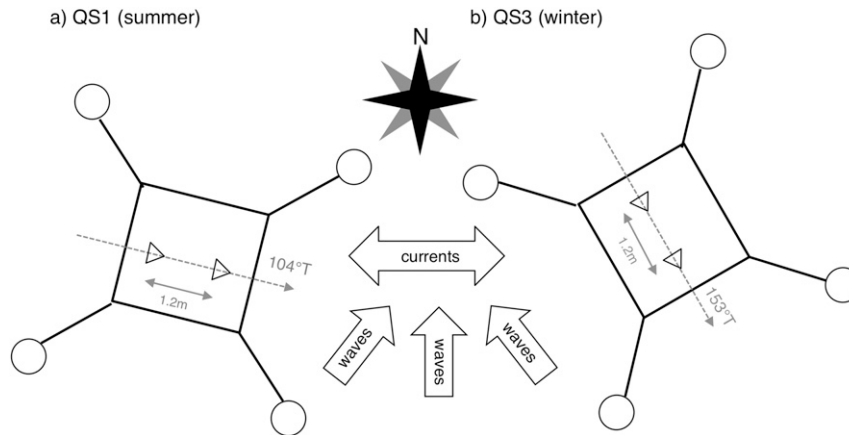FIG. 2. The quadpod being deployed from the University of Connecticut R/V *Connecticut*.

FIG. 3. Diagram showing the orientation of the quadpod and ADVs with the respect to the dominant current orientation and wave directions during deployments (a) QS1 and (b) QS3.

and ε is the dissipation rate for turbulent kinetic energy. The buoyancy frequency was estimated using the seawater equation of state (Fofonoff and Millard 1983) with the observed temperature differences and the array-averaged mean salinity, the conductivity cells having drifted sufficiently that differences between vertically separated conductivity measurements were not meaningful. The dissipation rate was estimated from inertial-range velocity autospectra using the method described by Scully et al. (2016).

3. Results

a. Model computations

Computations of the spatial structure of the turbulence, represented by $\int_{-\infty}^{+\infty} \Phi_{13}(\mathbf{k}) \, dk_3$, are similar but not identical (Figs. 4a,b) for the simple model (section 2a) and the rapid distortion model (appendix A). In both models, the dominant contribution to the cospectral density lies along the k_2 axis, but the details of the dependence on k_1 and k_2 differ.

Model computations of the frequency spectrum of the turbulence for an idealized wave spectrum (uniform within a finite frequency bandwidth) indicate strong dependence of the spectral shape on the model parameters. In particular, the shape of the cospectrum, including the breadth of the cospectral peak, changes significantly depending on whether the two sensors for the spatial differencing are aligned parallel or perpendicular to the mean current and whether the wave direction is parallel or perpendicular to the mean current (Fig. 5). The dependence of the model on the parameters is sufficiently complex that general features, even qualitative features, are difficult to predict in the absence of detailed numerical computations.

b. Model computations and laboratory measurements

At the uppermost height, the model computations and laboratory measurements of the along-stream correlation function $R_{13}^E(r_1, 0, 0)$ agree (Fig. 4c), indicating consistency of the laboratory measurements with the one-dimensional atmospheric expression (1), since $R_{13}^E(r_1, 0, 0)$ and $F_{13}(k_1)$ are a Fourier transform pair. At the lowermost height, the model computations and laboratory measurements of $R_{13}^E(r_1, 0, 0)$ agree less well, so that these measurements are less consistent with (1), possibly because of viscous effects, indicated by the smaller value of $x_3 u_*/\nu$, where u_* is the shear velocity, and ν is the molecular kinematic viscosity. The model computations of the cross-stream correlation function $R_{13}^E(0, r_2, 0)$ capture the main features of the measurements, that is, they change sign at approximately the correct value of r_2/λ, indicating a cross-stream correlation scale much shorter than the along-stream scale, although the modeled minima are not as deep as the measured minima (Fig. 4d). Note that the measured laboratory correlation functions are horizontally anisotropic, in that the scale in the cross-stream x_2 direction is significantly smaller than the scale in the along-stream x_1 direction and that both models capture this anisotropy.

c. Model computations and field measurements

The instruments experienced a range of conditions during the field deployments (Fig. 6). Wave heights ranged from approximately 0.5 m to more than 3 m, with dominant (spectral peak) wave periods typically between 5 and 10 s. Wave incidence was predominantly from the south during the first deployment and from the south and southwest during the second deployment. Near-bottom currents were predominantly east–west (parallel to the isobaths), with magnitudes of roughly $0.3 \, \mathrm{m \, s^{-1}}$,
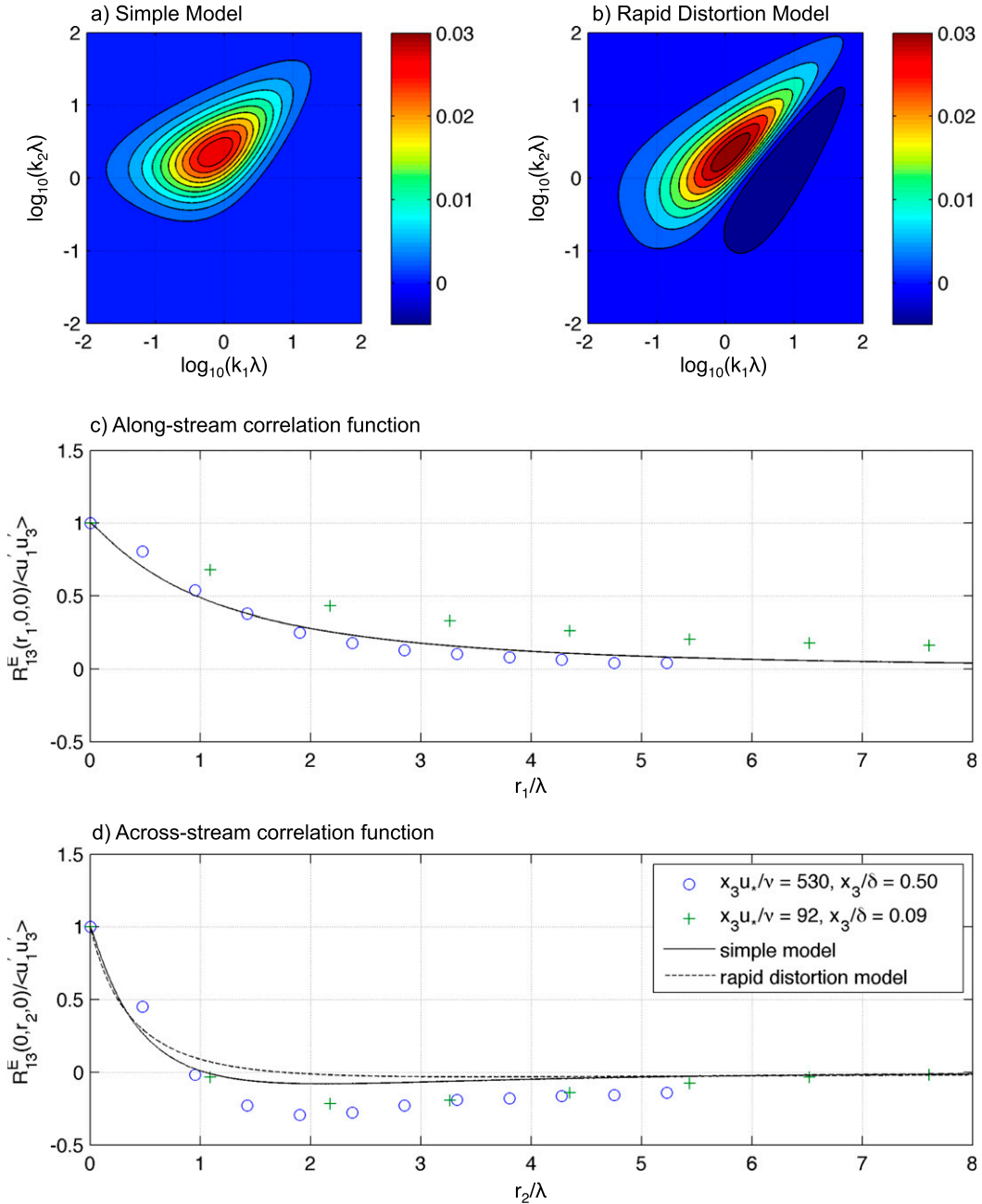
FIG. 4. Sample computations of $k_1 k_2 \int_{-\infty}^{+\infty} \Phi_{13}(\mathbf{k}) dk_3$ as a function of $\log_{10}(k_1\lambda)$ and $\log_{10}(k_2\lambda)$ based on (a) the simple model in section 2a and (b) the rapid distortion model in appendix A, together with model computations and laboratory measurements of the normalized (c) along-stream and (d) cross-stream correlation functions. In (a) and (b), the plots are in a covariance-preserving form, that is, the multiplication of $\int_{-\infty}^{+\infty} \Phi_{13}(\mathbf{k}) dk_3$ by k_1 and k_2 compensates for the logarithmic spacing of k_1 and k_2 according to $d\log(k_1) = dk_1/k_1$ and $d\log(k_2) = dk_2/k_2$.

dominated by semidiurnal tides, with occasional lower-frequency fluctuations of similar magnitude.

The variability in the cospectral estimates based on the measurements is sufficiently large that averages over the deployments, segregated by the ratio of the standard deviation of the wave velocity u_w to the current velocity

U_1, are most useful. As u_w/U_1 increases, the measured stress-carrying cospectrum shows pronounced departures from the shape that occurs under weak wave forcing (Figs. 7, 8), in particular declining at frequencies below the wave band and increasing at frequencies within and above the wave band. During the first
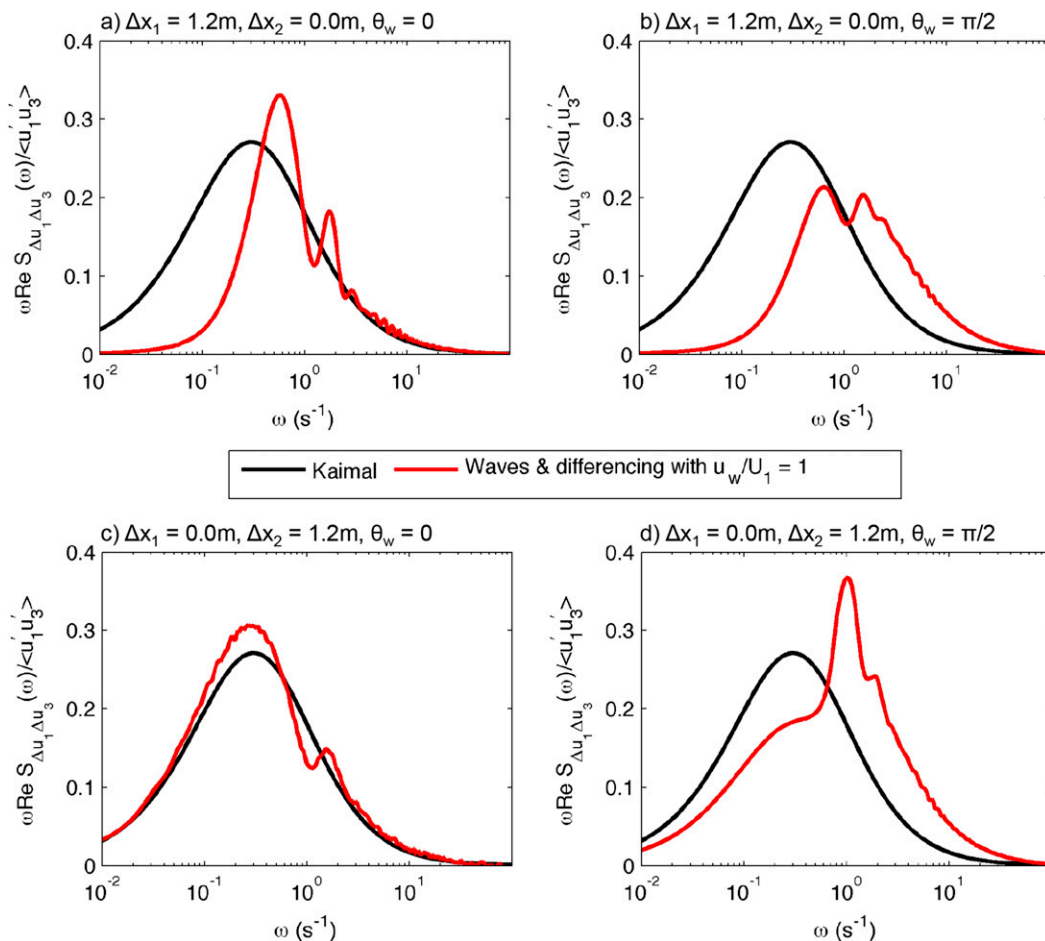
FIG. 5. Model computations of the shape of the frequency cospectrum of Δu_1 and Δu_3. In all computations, the mean current velocity U_1 is $0.3 \, \mathrm{m \, s^{-1}}$, the turbulent length scale λ is $0.5 \, \mathrm{m}$, the waves are unidirectional, and the frequency spectrum of the wave velocities is nonzero only within bands centered on $\omega_p = \pm 1 \, \mathrm{s^{-1}}$ with width $\Delta \omega = \omega_p / 2$ (i.e., a boxcar spectrum). The quantities θ_w and u_w are, respectively, the direction of the waves relative to the direction of the current (in radians) and the standard deviation of the wave velocity. The curves labeled Kaimal are twice (1) with $\omega = k_1 U_1$, consistent with the standard frozen turbulence approximation.

deployment (QS1), the simple model (section 2a) and to a lesser extent the model based on rapid distortion theory (appendix A) capture the observed distortion of the cospectrum (Fig. 7). During the second deployment (QS3), the performance of the simple model is slightly better than that of the rapid distortion model, but neither model captures the observed cospectral shape, even under relatively weak forcing. However, the models capture some of the qualitative features of the QS3 measurements, including enhancement in the wave band (although less than observed), and the model is quantitatively accurate at frequencies above the wave band. Quantification in terms of root-mean-square model data differences indicates that the simple model performs better than the rapid distortion model in almost all cases (Table 1). The best-fit values of the stress-carrying

turbulent scale λ indicate consistency with the Kaimal et al. (1972) result $\lambda \approx 1.5 x_3$ in the limit of negligible stratification, corresponding to $L_O \gg x_3$, and limitation to $\lambda \approx L_O$ in strong stratification, corresponding to $L_O \ll x_3$ (Fig. 9).

4. Discussion

The model computations are successful in reproducing the laboratory measurements (Fig. 4) and the main features of the field measurements during the first field deployment (Fig. 7), indicating that the assumptions underlying the models were satisfied in these measurements. The wavenumber spectrum of the turbulence is represented reasonably well by both the simple expression in section 2a and the more complex expressions
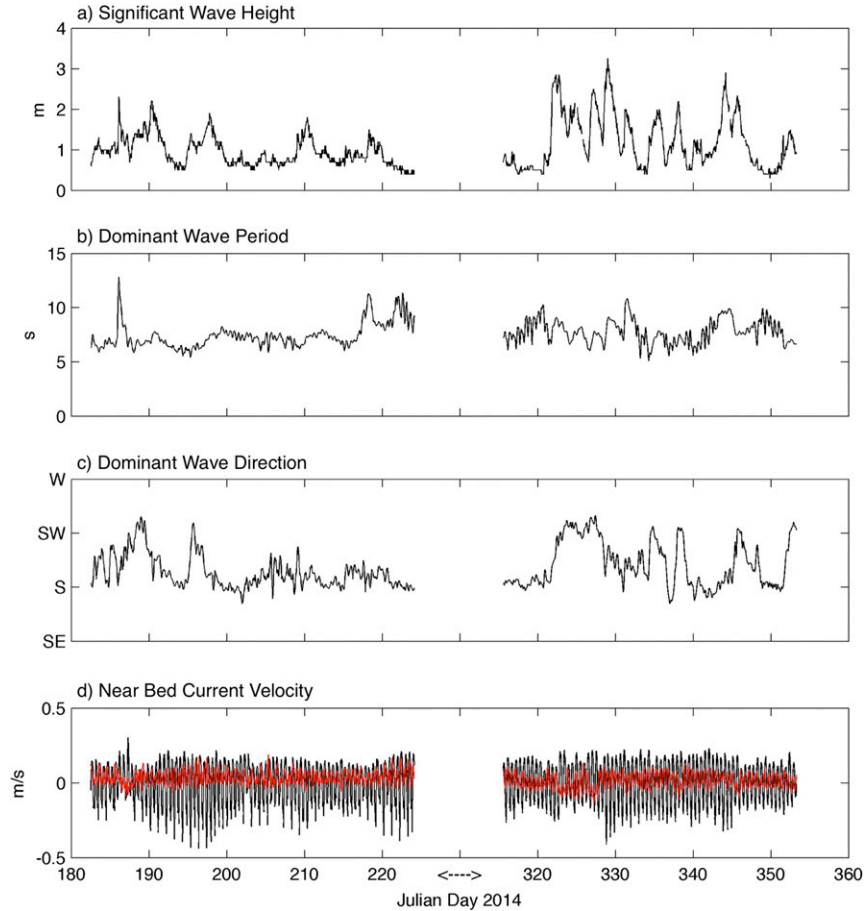
FIG. 6. Conditions during the measurement periods QS1 (days 183 to 223) and QS3 (days 316 to 354), including (a) significant wave height, (b) dominant wave period, (c) dominant wave direction (from), and (d) near-bed current velocity, with the alongshore component in black and the cross-isobath component in red.

in appendix A, and the distortion of the observed cospectrum in the presence of surface waves is largely the effect of advection of approximately frozen turbulence by the wave velocities.

The qualitatively correct but poorer quantitative performance of the models during the second field deployment (Fig. 8) is not understood. The model data comparison does not improve if the measurements are segregated based on $(\mathbf{k}_w \cdot \Delta \mathbf{x})^2 \theta \overline{\tilde{u}^2} \ll \overline{u'_1 u'_3}$, the theoretical criterion for the validity of the spatial differencing method (section 1), suggesting that possible shortcomings in the spatial differencing methodology do not explain the poorer model data agreement for the QS3 measurements. During the second deployment, convection likely occurred, evidenced by strong upward heat fluxes estimated from measurements at the Martha's Vineyard Coastal Observatory, and Langmuir circulations possibly occurred, evidenced by large skewness in fluctuations of vertical

velocity measured by the five-beam ADCP (Gargett et al. 2004). However, differences between observed and modeled cospectra did not increase systematically with metrics for convection and Langmuir circulation, suggesting that these processes, while important elsewhere in the water column, did not have a strong effect on the near-bottom dynamics of the stress-carrying turbulence and did not degrade the model data agreement. Similarly, the disagreement between observed and modeled cospectra did not depend consistently on the flow direction relative to the locations of the quadpod legs (Fig. 3), suggesting that flow disturbances by the quadpod are not responsible for the model data discrepancies. Finally, the model data agreement does not improve for the second deployment if flows from the west are excluded from the analysis, indicating that the proximity of the abrupt transition in seabed composition is not responsible for the discrepancies.
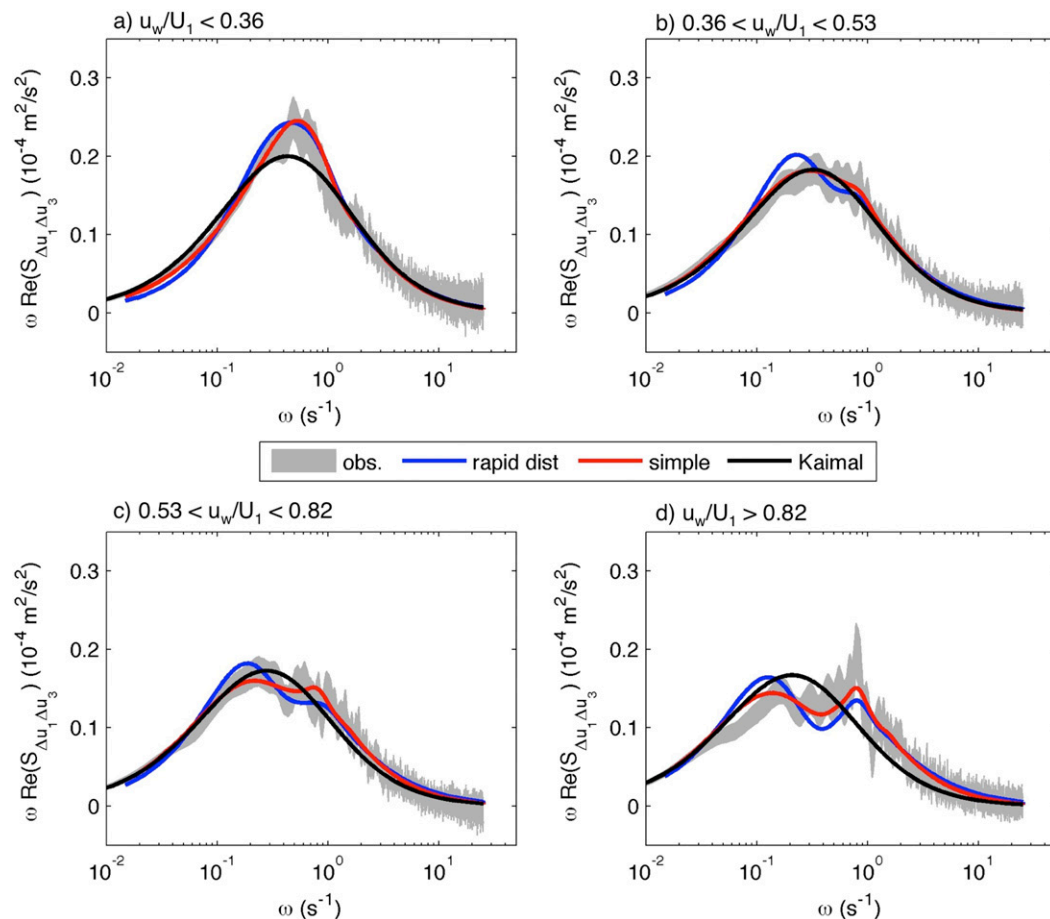
FIG. 7. Model data comparison for the summer deployment over coarse seafloor sediments (QS1), segregated by the ratio of the standard deviation of the wave velocity u_w to the current velocity U_1. The gray regions show the measurements with 95% confidence intervals for the cospectral estimates, the blue lines show computations based on the rapid distortion model (appendix A), the red lines show measurements based on the simple model (5), and the black lines show twice (1) with $\omega = k_1 U_1$. (a)–(d) Corresponds to quartiles of u_w/U_1. Table 1 shows the number of bursts in each quartile. Surface waves occur at radian frequencies ω of order unity, corresponding to dominant periods between 5 and 10 s (Fig. 6).

A possible reason for the observed model data discrepancies is a nonzero correlation between the turbulence and waves, which would be inconsistent with a fundamental assumption in the Lumley and Terray (1983) analysis. While possible, a significant correlation between the turbulence and waves is unlikely in the present application. The reasons are that wave nonlinearity (measured by the ratio of the near-bottom wave orbital velocity to the phase speed) is weak, the turbulence generated by wave breaking is unlikely to penetrate to the near-bottom measurement depth, and the turbulence and waves, while similar in temporal scales, have vastly different spatial scales (the distance above the boundary versus the inverse wavenumber of the surface waves), so that correlation of the two processes is unlikely.

The most likely explanation for the poorer quantitative performance of the model against the measured cospectra during the second deployment is inaccuracy of the underlying model of the spatial structure of the turbulence (section 2a). For the second deployment, the model does not capture the quantitative shapes of the measured cospectra even during relatively weak waves (Fig. 8a). The model representations of the spatial structure of the turbulence are likely less accurate in the cross-stream direction than in the along-stream direction, as indicated by the laboratory measurements (Fig. 4). The poorer model performance in Fig. 8, compared with Fig. 7, possibly results from the nearly cross-flow separation of the two ADVs in the second deployment (Fig. 3), so that the differencing operation likely compounded any model inaccuracies in the cross-stream direction.
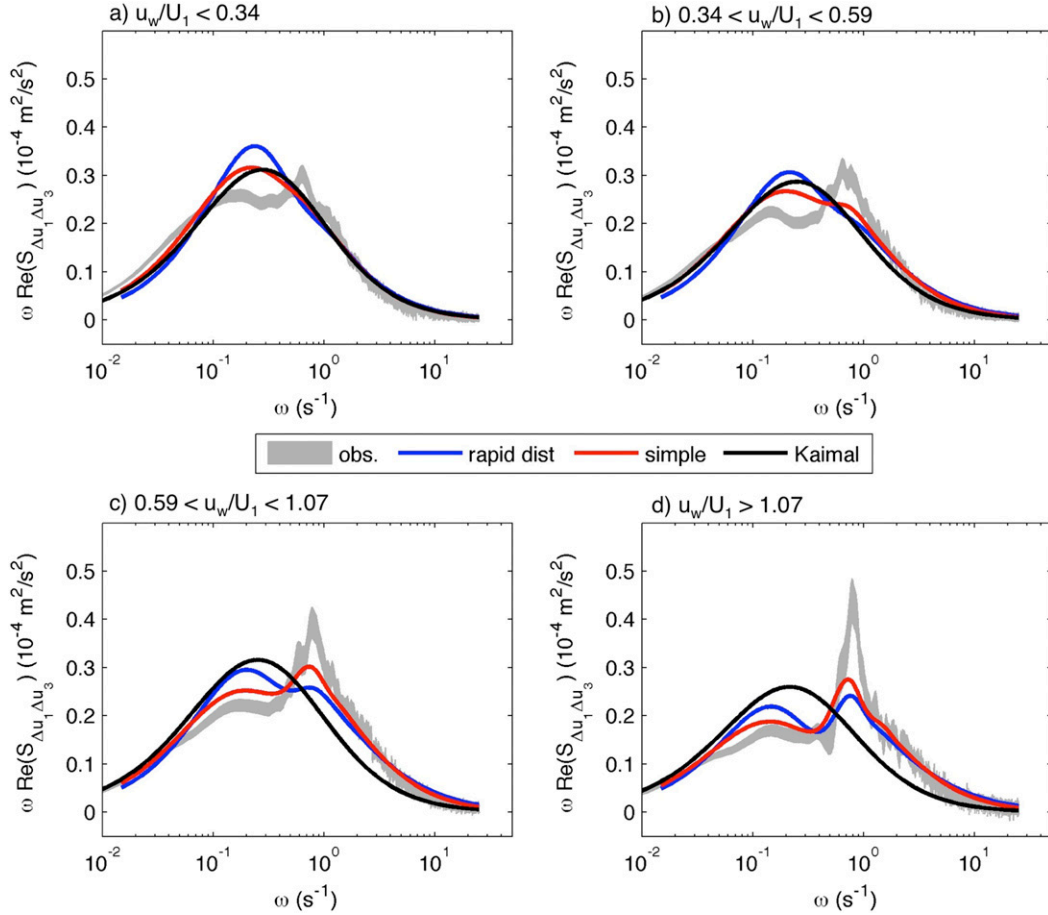
FIG. 8. As in Fig. 7, but for the fall and winter deployment over fine seafloor sediments (QS3).

However, the favorable agreement between model computations and measurements at high frequencies in both Figs. 7 and 8 suggests that the theoretically universal $k^{-7/3}$ behavior captured by (1) and also the simple (section 2a) and rapid distortion (appendix A) models of the turbulent structure are quantitatively sound.

In spite of the possible model deficiencies regarding the spatial structure of the turbulence, the best-fit estimates of the turbulent length scale λ (Fig. 9) are

TABLE 1. Root-mean-square difference ($10^{-6}\,\mathrm{m^2\,s^{-2}}$) between observations and model computations of radian frequency ω times cospectral density $\mathrm{Re}[S_{\Delta u_1 \Delta u_3}(\omega)]$, arranged by quartiles of u_w/U_1, as in Figs. 7 and 8. RDT indicates rapid distortion theory, and n is the number of 28-min bursts for each entry.

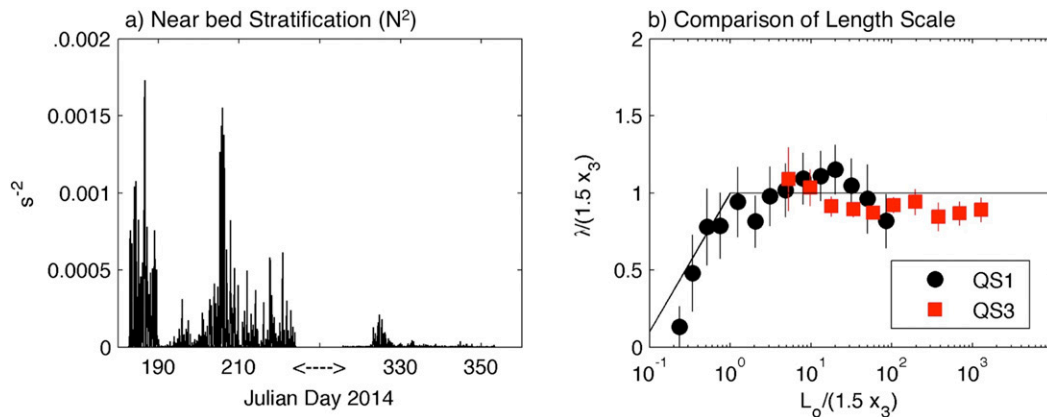| First deployment (QS1)			
$u_w/U_1 < 0.36$	$0.36 < u_w/U_1 < 0.53$	$0.53 < u_w/U_1 < 0.82$	$u_w/U_1 > 0.82$
$n = 135$	$n = 135$	$n = 135$	$n = 135$
Simple model 0.98	0.59	0.80	1.30
RDT model 1.22	1.26	1.14	2.10
Kaimal model 1.43	1.26	1.08	2.46
Second deployment (QS3)			
$u_w/U_1 < 0.34$	$0.34 < u_w/U_1 < 0.59$	$0.59 < u_w/U_1 < 1.07$	$u_w/U_1 > 1.07$
$n = 397$	$n = 397$	$n = 397$	$n = 397$
Simple model 2.81	2.97	2.59	3.45
RDT model 4.49	4.50	4.51	4.49
Kaimal model 2.74	4.12	6.64	7.95

FIG. 9. (a) Near-bed stratification N^2, where N is the buoyancy frequency and (b) binned-mean best-fit values of the turbulent length scale λ as a function of the height x_3 above the bottom and the Ozmidov scale L_O. In (b), the data are averaged in bins of $L_O/(1.5x_3)$, and the error bars show plus and minus two standard errors, corresponding approximately to 95% confidence intervals; $\lambda/(1.5x_3) = 1$ corresponds to the Kaimal et al. (1972) model [(1)] at neutral stratification; and the solid line shows equality for $L_O/(1.5x_3) < 1$ and a threshold for $L_O/(1.5x_3) > 1$.

consistent with expectations based on classical conceptions of stratified turbulence, as found in previous nearshore and estuarine studies (Trowbridge and Elgar 2003; Scully et al. 2011). It is noteworthy that stratification has a measurable effect on turbulence even at heights above bottom as small as 0.5 m.

5. Summary and conclusions

The present study has shown that relatively simple models of boundary layer turbulence, combined with an analysis of the advection of frozen turbulence by random surface waves, reproduce the main features of stress-carrying cospectra measured near the seafloor in the coastal ocean during one field deployment and, with less quantitative success, the main features of the cospectrum during a second deployment. A possible reason for the greater model data differences during the second deployment is potentially inaccurate model representation of the cross-stream structure of the stress-carrying turbulent wavenumber cospectrum, accentuated by spatial differencing in that direction, accentuated by the wave advection in the same direction. Model computations were quantitatively consistent with measurements at high frequencies (above the wave band) during both deployments, suggesting that the underlying turbulence model at high wavenumbers, founded in established theoretical concepts, is sound. The effect of stable stratification on the stress-carrying turbulent length scale is quantitatively consistent with expectations during both deployments.

APPENDIX A

A Model of Φ_{13} Based on Rapid Distortion Theory

The expression for $\Phi_{13}(\mathbf{k})$ from the small-time asymptote of the rapid distortion solution for initially isotropic turbulence in mean shear (Townsend 1980) can be written as

$$\Phi_{13}(\mathbf{k}) = \frac{15}{16\pi} \frac{E(k)}{k^2} \left(\frac{k_2^2 - k_1^2}{k^2} + 4 \frac{k_1^2 k_3^2}{k^4} \right) \overline{u_1' u_3'}. \quad \text{(A1)}$$

Here, $k = |\mathbf{k}|$ is the magnitude of the wavenumber; $E(k)$ is the scalar wavenumber spectrum of the initially isotropic turbulence, normalized so that $\int_0^{+\infty} E(k)\, dk = 1$; the factor $15/(16\pi)$ ensures that $\int \Phi_{13}(\mathbf{k})\, d\mathbf{k} = \overline{u_1' u_3'}$; the term that represents the initially isotropic turbulence has been neglected because it is odd in k_3 and does not

contribute to the present results; and a factor of k^2 in the numerator beneath $E(k)$, missing in the Townsend (1980) expression, has been restored.

The quantity $E(k)$ in (A1) is modeled by requiring consistency with the semiempirical expression (1). Substitution of (A1) into (4) yields an expression that can be reduced to a single integral by introducing cylindrical coordinates $\mathbf{k} = [k_1, s\cos(\phi), s\sin(\phi)]$ and integrating in ϕ from zero to 2π. The result is

$$F_{13}(k_1) = \frac{15}{16}\overline{u_1 u_3}\int_0^{+\infty} s\,ds\left(s^2 - 2k_1^2 + 4s^2\frac{k_1^2}{k^2}\right)\frac{E(k)}{k^4},$$
(A2)

where $k = \sqrt{k_1^2 + s^2}$ in the integrand. Following Batchelor (1953), change the integration variable in (A2) from s to k, noting that $k\,dk = s\,ds$ and that $s = 0$ corresponds to $k = |k_1|$. After substitution of (1), the result for positive k_1 is

$$\frac{15}{16}\int_{|k_1|}^{+\infty} E(k)\left(\frac{1}{k} + \frac{k_1^2}{k^3} - 4\frac{k_1^4}{k^5}\right)dk = F(k_1) = \frac{2}{3}\frac{\lambda}{(1 + |k_1|\lambda)^{7/3}}.$$
(A3)

To invert for $E(k)$, differentiate (A3) three times with respect to k_1 using the Leibniz rule, multiply the derivatives by factors chosen to eliminate the integrals, and then sum. The result is

$$k\frac{\partial}{\partial k}\left(k\frac{\partial E}{\partial k}\right) + k\frac{\partial E}{\partial k} - 4E = G(k),$$
(A4)

where

$$G(k) = \frac{8}{15}k^3\frac{d^3 F}{dk^3} - \frac{8}{5}k^2\frac{d^2 F}{dk^2} + \frac{8}{5}k\frac{dF}{dk}.$$
(A5)

The solution of (A4) that is finite at small and large k is

$$E(k) = \frac{1}{\mu_- - \mu_+}\left[k^{\mu_-}\int_0^k k_1^{\mu_+}G(k_1)\,dk_1 + k^{\mu_+}\int_k^{+\infty} k_1^{\mu_-}G(k_1)\,dk_1\right],$$
(A6)

or

$$E(k) = \frac{1}{\mu_- - \mu_+}\int_0^{+\infty}\min(k^{\mu_-}k_1^{\mu_+}, k^{\mu_+}k_1^{\mu_-})G(k_1)\,dk_1,$$
(A7)

where $\mu_+ = (-1 + \sqrt{17})/2$ and $\mu_- = (-1 - \sqrt{17})/2$. The model for $\Phi_{13}(\mathbf{k})$ is (A1), with $E(k)$ determined by (A5) and (A7). The model parameters are $\overline{u_1' u_3'}$ and λ. Checks

on the numerical computations of $E(k)$ are the normalization $\int_0^{+\infty} E(k)dk = 1$ and consistency with (A3).

Introduce cylindrical coordinates $\mathbf{k} = [\xi\cos(\theta), \xi\sin(\theta), k_3]$, so that (A1) becomes

$$\Phi_{13}(\mathbf{k}) = \frac{15}{16\pi}\frac{E(k)}{k^2}\left[2\frac{\xi^2 k_3^2}{k^4} + \left(2\frac{\xi^2 k_3^2}{k^4} - \frac{\xi^2}{k^2}\right)\cos(2\theta)\right]\overline{u_1' u_3'}.$$
(A8)

The k_3 integral can be written as

$$\int_{-\infty}^{+\infty}\Phi_{13}(\mathbf{k})\,dk_3 = [A_0(\xi) + A_2(\xi)\cos(2\theta)]\overline{u_1' u_3'},$$
(A9)

where

$$A_0(\xi) = \frac{15}{4\pi}\xi^2\int_0^{+\infty}\frac{k_3^2 E(k)}{k^6}dk_3, \quad \text{and}$$
(A10)

$$A_2(\xi) = \frac{15}{4\pi}\xi^2\int_0^{+\infty}\left(\frac{k_3^2}{k^6} - \frac{1}{2k^4}\right)E(k)\,dk_3,$$
(A11)

with $k = \sqrt{k_3^2 + \xi^2}$ in the integrands. The quantities $R_{13}^E(r_1, r_2, 0)$, $\rho_{\Delta u_1 \Delta u_3}(\tau)$, and $S_{\Delta u_1 \Delta u_3}(\omega)$ are computed by substituting (A9), (A10), and (A11) into (6), (8), and (9) and evaluating numerically. Checks on the calculations are $2\pi\int_0^{+\infty}\xi A_0(\xi)d\xi = 1$, from $R_{13}(0, 0, 0) = \overline{u_1' u_3'}$, and $\int_0^{+\infty}[A_0(\xi) + A_2(\xi)]d\xi = 0$, from $\int_0^{+\infty} R_{13}(0, r_2, 0)dr_2 = 0$; a consequence of continuity (Batchelor 1953) in the rapid distortion model.

APPENDIX B

Derivation of (9)

The starting point is the Fourier–Stieltjes integral representation of the ith component of the turbulent velocity (Batchelor 1953; Monin and Yaglom 1975):

$$u_i'(\mathbf{x}, t) = \int d\hat{u}_i(\mathbf{k}, t)\,e^{\imath\mathbf{k}\cdot\mathbf{x}}.$$
(B1)

Here, $d\hat{u}_i$ is the complex Fourier–Stieltjes amplitude, and the integral is over all of the three-dimensional wavenumber space. In the frozen turbulence approximation, following Lumley and Terray (1983), the time dependence of the amplitude is suppressed, and the time dependence of the velocity is represented by the incorporation of the flow-induced displacement into the complex exponential:

$$u_i'(\mathbf{x}, t) = \int d\hat{u}_i(\mathbf{k})\,e^{\imath\mathbf{k}\cdot\mathbf{x} + \imath\mathbf{k}\cdot\mathbf{U}t + \imath\mathbf{k}\cdot\mathbf{X}(t)}.$$
(B2)

Here, $\mathbf{U}t$ is the displacement caused by the current, $\mathbf{X}(t) = \int \tilde{\mathbf{u}} dt$ is the displacement caused by the surface waves, and advection by the turbulence is assumed to be negligible. The velocity at $\mathbf{x} + \Delta\mathbf{x}$ is

$$u_i'(\mathbf{x} + \Delta\mathbf{x}, t) = \int d\hat{u}_i(\mathbf{k}) \, e^{\iota \mathbf{k}\cdot\mathbf{x} + \iota \mathbf{k}\cdot\Delta\mathbf{x} + \iota \mathbf{k}\cdot\mathbf{U}t + \iota \mathbf{k}\cdot\mathbf{X}(t)}. \quad \text{(B3)}$$

The difference between (B3) and (B2) is

$$\Delta u_i'(t) = u_i'(\mathbf{x} + \Delta\mathbf{x}, t) - u_i'(\mathbf{x}, t)$$
$$= \int d\hat{u}_i(\mathbf{k}) \, e^{\iota \mathbf{k}\cdot\mathbf{x} + \iota \mathbf{k}\cdot\mathbf{U}t + \iota \mathbf{k}\cdot\mathbf{X}(t)}(e^{\iota \mathbf{k}\cdot\Delta\mathbf{x}} - 1). \quad \text{(B4)}$$

Since this quantity is real, it is equal to its own complex conjugate:

$$\Delta u_i'(t) = \int d\hat{u}_{i*}(k') \, e^{-\iota k'\cdot\mathbf{x} - \iota k'\cdot\mathbf{U}t - \iota k'\cdot\mathbf{X}(t)}(e^{-\iota k'\cdot\Delta\mathbf{x}} - 1), \quad \text{(B5)}$$

where asterisks denote complex conjugation, and $\mathbf{k}'$, like $\mathbf{k}$ in the preceding expressions, is a dummy integration variable. Using (B4), the jth component of the velocity difference at time $t + \tau$ can be written

$$\Delta u_j'(t + \tau) = \int d\hat{u}_j(\mathbf{k}) \, e^{\iota \mathbf{k}\cdot\mathbf{x} + \iota \mathbf{k}\cdot\mathbf{U}t + \iota \mathbf{k}\cdot\mathbf{U}\tau + \iota \mathbf{k}\cdot\mathbf{X}(t+\tau)}(e^{\iota \mathbf{k}\cdot\Delta\mathbf{x}} - 1).$$
$$\text{(B6)}$$

The temporal covariance function, obtained by multiplying (B5) and (B6) and taking the expected value, is

$$\rho_{\Delta u_i \Delta u_j}(\tau) = \iint \overline{d\hat{u}_{i*}(\mathbf{k}') \, d\hat{u}_j(\mathbf{k})} \, e^{\iota(\mathbf{k}-\mathbf{k}')\cdot(\mathbf{x}+\mathbf{U}t) + \iota \mathbf{k}\cdot\mathbf{U}\tau} \, \overline{e^{\iota[\mathbf{k}\cdot\mathbf{X}(t+\tau) - \mathbf{k}'\mathbf{X}(t)]}} [e^{\iota(\mathbf{k}-\mathbf{k}')\cdot\Delta\mathbf{x}} - e^{\iota \mathbf{k}\cdot\Delta\mathbf{x}} - e^{-\iota k'\cdot\Delta\mathbf{x}} + 1]. \quad \text{(B7)}$$

Here, the integral is over all of the six-dimensional $\mathbf{k}$ and $\mathbf{k}'$ space, and the statistical independence of the waves and currents has been invoked to separate the two expected values. The first term in the integral in (B7) is related to the wavenumber spectrum $\Phi_{ij}(\mathbf{k})$ by (Batchelor 1953; Monin and Yaglom 1975)

$$\overline{d\hat{u}_{i*}(\mathbf{k}') \, d\hat{u}_j(\mathbf{k})} = \Phi_{ij}(\mathbf{k}) d\mathbf{k} \delta(\mathbf{k} - \mathbf{k}') d\mathbf{k}, \quad \text{(B8)}$$

where δ is the Dirac delta function (not to be confused with the boundary layer thickness, as in sections 2 and 3). Substitution of (B8) into (B7) gives

$$\rho_{\Delta u_i \Delta u_j}(\tau) = 2 \int \Phi_{ij}(\mathbf{k}) \, e^{\iota \mathbf{k}\cdot\mathbf{U}\tau} \overline{e^{\iota \mathbf{k}\cdot[\mathbf{X}(t+\tau)-\mathbf{X}(t)]}} [1 - \cos(\mathbf{k}\cdot\Delta\mathbf{x})] \, d\mathbf{k}.$$
$$\text{(B9)}$$

The expected value in the integral in (B9) is the characteristic function of $\mathbf{X}(t + \tau) - \mathbf{X}(t)$ (e.g., Lumley 1998). For Gaussian wave statistics (as as-sumed), this quantity can be written (Lumley and Terray 1983)

$$\overline{e^{\iota \mathbf{k}\cdot[\mathbf{X}(t+\tau)-\mathbf{X}(t)]}} = e^{-k_m k_n[\overline{X_m X_n} - \overline{X_m(t)X_n(t+\tau)}]}, \quad \text{(B10)}$$

where the summation convention applies; that is, the right side of (B10) is understood to be summed over all three values of m and n. The quantity $\overline{X_m(t)X_n(t + \tau)}$ is the temporal covariance function of the wave displacements, expressible as the inverse Fourier transform of the frequency spectrum $S_{X_m X_n}(\sigma)$:

$$\overline{X_m(t)X_n(t + \tau)} = \int_{-\infty}^{+\infty} S_{X_m X_n}(\sigma) \, e^{\iota \sigma \tau} \, d\sigma, \quad \text{(B11)}$$

where σ is a dummy radian frequency. After use of (B10) and (B11), the relationship $S_{\tilde{u}_m \tilde{u}_n}(\sigma) = \sigma^2 S_{X_m X_n}(\sigma)$, the trigonometric identity $1 - \cos(\sigma\tau) = 2\sin^2(\sigma\tau/2)$, and symmetries eliminate the imaginary part of (B11), (B9) becomes

$$\rho_{\Delta u_i \Delta u_j}(\tau) = 2 \int \Phi_{ij}(\mathbf{k}) \, e^{\iota \mathbf{k}\cdot\mathbf{U}\tau} \exp\left[-\frac{\tau^2}{2} k_m k_n \int_{-\infty}^{+\infty} S_{\tilde{u}_m \tilde{u}_n}(\sigma) \frac{\sin^2(\sigma\tau/2)}{(\sigma\tau/2)^2} \, d\sigma \right] [1 - \cos(\mathbf{k} \cdot \Delta\mathbf{x})] \, d\mathbf{k}. \quad \text{(B12)}$$

Substitution of $i = 1$ and $j = 3$ into (B12) yields (9).

REFERENCES

Ackerman, S. D., L. L. Brothers, D. S. Foster, B. D. Andrews, W. E. Baldwin, and W. C. Schwab, 2016: High-resolution geophysical data from the inner continental shelf: South of Martha's Vineyard and north of Nantucket, Massachusetts. U.S. Geological Survey Open-File Rep. 2016-1168, 21 pp., https://doi.org/10.3133/ofr20161168.

Batchelor, G. K., 1953: *The Theory of Homogeneous Turbulence.* Cambridge University Press, 197 pp.

Cambon, C., and J. F. Scott, 1999: Linear and nonlinear models of anisotropic turbulence. *Annu. Rev. Fluid Mech.*, **31**, 1–53, https://doi.org/10.1146/annurev.fluid.31.1.1.

Craik, A. D. D., and S. Leibovich, 1976: A rational theory for Langmuir circulation. *J. Fluid Mech.*, **73**, 401–426, https://doi.org/10.1017/S0022112076001420.

Denny, J. F., W. W. Danforth, D. S. Foster, and C. R. Sherwood, 2009: Geophysical data collected off the south shore of Martha's Vineyard, Massachusetts. U.S. Geological Survey Open-File Rep. 2008-1288, https://pubs.er.usgs.gov/publication/ofr20081288.

Elgar, S., B. Raubenheimer, and R. T. Guza, 2005: Quality control of acoustic Doppler velocimeter data in the surfzone. *Meas. Sci. Technol.*, **16**, 1889–1893, https://doi.org/10.1088/0957-0233/16/10/002.

Feddersen, F., 2010: Quality controlling surf zone acoustic Doppler velocimeter observations to estimate the turbulent dissipation rate. *J. Atmos. Oceanic Technol.*, **27**, 2039–2055, https://doi.org/10.1175/2010JTECHO783.1.

——, 2012: Observations of the surf-zone turbulent dissipation rate. *J. Phys. Oceanogr.*, **42**, 386–399, https://doi.org/10.1175/JPO-D-11-082.1.

——, and A. J. Williams, 2007: Direct estimation of the Reynolds stress vertical structure in the nearshore. *J. Atmos. Oceanic Technol.*, **24**, 102–116, https://doi.org/10.1175/JTECH1953.1.

——, J. H. Trowbridge, and A. J. Williams, 2007: Vertical structure of dissipation in the nearshore. *J. Phys. Oceanogr.*, **37**, 1764–1777, https://doi.org/10.1175/JPO3098.1.

Fofonoff, N. P., and R. C. Millard Jr., 1983: Algorithms for computation of fundamental properties of seawater. UNESCO Tech. Paper in Marine Science 44, 53 pp., http://unesdoc.unesco.org/images/0005/000598/059832eb.pdf.

Ganapathisubramani, B., N. Hutchins, W. T. Hambleton, E. K. Longmire, and I. Marusic, 2005: Investigation of large-scale coherence in a turbulent boundary layer using two-point correlations. *J. Fluid Mech.*, **524**, 57–80, https://doi.org/10.1017/S0022112004002277.

Gargett, A., and J. R. Wells, 2007: Langmuir turbulence in shallow water. Part 1. Observations. *J. Fluid Mech.*, **576**, 27–61, https://doi.org/10.1017/S0022112006004575.

——, ——, A. E. Tejada-Martínez, and C. E. Grosch, 2004: Langmuir supercells: A mechanism for sediment resuspension and transport in shallow seas. *Science*, **306**, 1925–1928, https://doi.org/10.1126/science.1100849.

Gerbi, G. P., J. H. Trowbridge, J. B. Edson, A. J. Plueddemann, E. A. Terray, and J. J. Fredericks, 2008: Measurements of momentum and heat transfer across the air–sea interface. *J. Phys. Oceanogr.*, **38**, 1054–1072, https://doi.org/10.1175/2007JPO3739.1.

——, ——, E. A. Terray, A. J. Plueddemann, and T. Kukulka, 2009: Observations of turbulence in the ocean surface boundary layer: Energetics and transport. *J. Phys. Oceanogr.*, **39**, 1077–1096, https://doi.org/10.1175/2008JPO4044.1.

Grant, W. D., and O. S. Madsen, 1979: Combined wave and current interaction with a rough bottom. *J. Geophys. Res.*, **84**, 1797–1807, https://doi.org/10.1029/JC084iC04p01797.

——, and ——, 1986: The continental-shelf bottom boundary layer. *Annu. Rev. Fluid Mech.*, **18**, 265–305, https://doi.org/10.1146/annurev.fl.18.010186.001405.

Hunt, J. C. R., and D. J. Carruthers, 1990: Rapid distortion theory and the 'problems' of turbulence. *J. Fluid Mech.*, **212**, 497–532, https://doi.org/10.1017/S0022112090002075.

Jeffreys, H., 1931: *Cartesian Tensors.* Cambridge University Press, 92 pp.

Kaimal, J. C., J. C. Wyngaard, Y. Izumi, and O. R. Cote, 1972: Spectral characteristics of surface layer turbulence. *Quart. J. Roy. Meteor. Soc.*, **98**, 563–589, https://doi.org/10.1002/qj.49709841707.

Longuet-Higgins, M. S., 1953: Mass transport in water waves. *Philos. Trans. Roy. Soc. London*, **A245**, 535–581, https://doi.org/10.1098/rsta.1953.0006.

Lumley, J. L., 1998: *Stochastic Tools in Turbulence.* Academic Press, 194 pp.

——, and E. A. Terray, 1983: Kinematics of turbulence convected by a random wave field. *J. Phys. Oceanogr.*, **13**, 2000–2007, https://doi.org/10.1175/1520-0485(1983)013<2000:KOTCBA>2.0.CO;2.

Monin, A. S., and A. M. Yaglom, 1975: *Statistical Fluid Mechanics: Mechanics of Turbulence.* Vol. 2. MIT Press, 896 pp.

Montgomery, E. T., C. R. Sherwood, M. A. Martini, J. Trowbridge, M. Scully, and S. M. Brosnahan, 2016: Oceanographic and water-quality measurements collected south of Martha's Vineyard, MA, 2014–2015. U.S. Geological Survey, https://doi.org/10.5066/F7542KQR.

Phillips, O. M., 1980: *The Dynamics of the Upper Ocean.* 2nd ed. Cambridge University Press, 336 pp.

Priestley, M. B., 1981: *Spectral Analysis and Time Series.* Academic Press, 890 pp.

Rosman, J. H., and G. P. Gerbi, 2017: Interpreting fixed-location observations of turbulence advected by waves: Insights from spectral models. *J. Phys. Oceanogr.*, **47**, 909–931, https://doi.org/10.1175/JPO-D-15-0249.1.

Ruessink, B. G., 2010: Observations of turbulence within a natural surf zone. *J. Phys. Oceanogr.*, **40**, 2696–2712, https://doi.org/10.1175/2010JPO4466.1.

Savill, A. M., 1987: Recent developments in rapid-distortion theory. *Annu. Rev. Fluid Mech.*, **19**, 531–575, https://doi.org/10.1146/annurev.fl.19.010187.002531.

Schlichting, H., and K. Gersten, 2000: *Boundary-Layer Theory.* 8th ed. Springer, 801 pp.

Scully, M. E., W. R. Geyer, and J. H. Trowbridge, 2011: The influence of stratification and nonlocal turbulent production on estuarine turbulence: An assessment of turbulence closure with field observations. *J. Phys. Oceanogr.*, **41**, 166–185, https://doi.org/10.1175/2010JPO4470.1.

——, J. H. Trowbridge, and A. W. Fisher, 2016: Observations of the transfer of energy and momentum to the oceanic surface boundary layer beneath breaking waves. *J. Phys. Oceanogr.*, **46**, 1823–1837, https://doi.org/10.1175/JPO-D-15-0165.1.

Shaw, W. J., and J. H. Trowbridge, 2001: The direct estimation of near-bottom turbulent fluxes in the presence of energetic wave motions. *J. Atmos. Oceanic Technol.*, **18**, 1540–1557, https://doi.org/10.1175/1520-0426(2001)018<1540:TDEONB>2.0.CO;2.

Tennekes, H., and J. L. Lumley, 1972: *A First Course in Turbulence.* MIT Press, 300 pp.

Terray, E. A., M. A. Donelan, Y. C. Agrawal, W. M. Drennan, K. K. Kahma, A. J. Williams, P. A. Hwang, and

S. A. Kitaigorodskii, 1996: Estimates of kinetic energy dissipation under breaking waves. *J. Phys. Oceanogr.*, **26**, 792–807, https://doi.org/10.1175/1520-0485(1996)026<0792:EOKEDU>2.0.CO;2.

Townsend, A. A., 1980: *The Structure of Turbulent Shear Flow.* Cambridge University Press, 429 pp.

Tritton, D. J., 1967: Some new correlation measurements in a turbulent boundary layer. *J. Fluid Mech.*, **28**, 439–462, https://doi.org/10.1017/S0022112067002216.

Trowbridge, J., 1998: On a technique for measuring turbulent shear stress in the presence of surface waves. *J. Atmos. Oceanic Technol.*, **15**, 290–298, https://doi.org/10.1175/1520-0426(1998)015<0290:OATFMO>2.0.CO;2.

——, and S. Elgar, 2001: Turbulence measurements in the surf zone. *J. Phys. Oceanogr.*, **31**, 2403–2417, https://doi.org/10.1175/1520-0485(2001)031<2403:TMITSZ>2.0.CO;2.

——, and ——, 2003: Spatial scales of stress-carrying nearshore turbulence. *J. Phys. Oceanogr.*, **33**, 1122–1128, https://doi.org/10.1175/1520-0485(2003)033<1122:SSOSNT>2.0.CO;2.

Wyngaard, J. C., and O. R. Cote, 1972: Cospectral similarity in the atmospheric surface layer. *Quart. J. Roy. Meteor. Soc.*, **98**, 590–603, https://doi.org/10.1002/qj.49709841708.